The Photocatalyst Activity of Hematite Nanocrystals Prepared by The Sol-Gel Method

Maulidina, Hikmah
Department of Physics, Faculty of Mathematics and Natural Sciences, Universitas Sebelas Maret

Ananda Sholeh Rifky Hakim
Department of Physics, Faculty of Mathematics and Natural Sciences, Universitas Sebelas Maret

Utari
Department of Physics, Faculty of Mathematics and Natural Sciences, Universitas Sebelas Maret

Purnama, Budi
Department of Physics, Faculty of Mathematics and Natural Sciences, Universitas Sebelas Maret

https://doi.org/10.5109/7236872

出版情報：Evergreen. 11 (3), pp.2296-2304, 2024-09. 九州大学グリーンテクノロジー研究教育センター
バージョン：

EVERGREEN Joint Journal of Novel Carbon Resource Sciences & Green Asia Strategy, Vol. 11, Issue 03, pp2296-2304, September, 2024

The Photocatalyst Activity of Hematite Nanocrystals Prepared by The Sol-Gel Method

Hikmah Maulidina, Ananda Sholeh Rifky Hakim, Utari, Budi Purnama*
Department of Physics, Faculty of Mathematics and Natural Sciences, Universitas Sebelas Maret,
Jl. Ir Sutami 36A Kentingan Jebres Surakarta 57126, Indonesia

*Author to whom correspondence should be addressed:
E-mail: hikmahmauliddina@gmail.com, bpurnama@mipa.uns.ac.id

(Received October 30, 2023; Revised June 5, 2024; Accepted September 7, 2024).

Abstract: In this study, iron oxide hematite (α-Fe_2O_3) nanocrystals were prepared using nonahydrate ferrite nitrate and citric acid monohydrate as the precursors. Toward change in the physical properties of the resulting product, annealing was performed at 400, 500, 600, and 700°C for 4 h. The hematite (α-Fe_2O_3) samples were characterized by FTIR spectroscopy, XRD, and SEM. The FTIR data displayed primary Fe-O vibrations, that the sample implies as hematite (α-Fe_2O_3). The XRD and SEM results confirmed an increase in the crystallite size with increasing annealing temperature. Furthermore, the crystallite size range from 25.9-46.1 nm. The magnetic properties of the samples were evaluated using VSM. The hematite (α-Fe_2O_3) nanocrystals were exposed to the photodegradation of blue methylene under UV light irradiation. Photocatalysts with 60 mg of hematite (α-Fe_2O_3) without annealing treatment were found to have the highest degradation efficiency of blue methylene until 90.04% compared to other doses. Finally, the increase in the dye degradation efficiency with the increment of hematite (α-Fe_2O_3) nanocrystals indicates the reduction of the dye support by surface adsorption following the photocatalysis mechanism.

Keywords: hematite (α-Fe_2O_3); sol-gel; photocatalyst

1. Introduction

Hematite (α-Fe_2O_3) has been widely researched and is the most stable ion with a hexagonal structure, has semi-conductive properties (type n) in environmental conditions, and has a high resistance to corrosion. The low-cost, non-toxic, and widely used treatment of hematite (α-Fe_2O_3) in many applications, for instance, in coloring pigments[1,2)], lithium-ion batteries[3)], gas sensors[4,5)], catalytic biomedical devices[6,7)], water purification[8)], and solar energy conservation[9,10)], has made hematite (α-Fe_2O_3) nanocrystals the most popular investigation of all iron oxides. Hematite (α-Fe_2O_3) nanocrystals have been prepared using various synthesis methods[11,12)], such as the sol-gel method[13-15)], solvothermal method[16,17)], thermal and hydrothermal pyrolysis[18)], combustion[19)], co-precipitation method[20,21)], and alloying methods using natural iron-oxide fine sediment[22]. The sol-gel method has great potential method for obtaining advanced metal-oxide materials. The crystallinity, size, and properties of hematite can be tuned by the annealing temperature making it an important parameter [23-26)]. Hematite has a very small size compared to other nanoparticles. Thus, providing a large surface area within result, hematite is one of the best pollutant-absorbing materials. Moreover, hematite attracts and binds pollutants, including metals, organic dyes and pharmaceutical contaminants[27)]. In this research, hematite (α- Fe_2O_3) nanocrystals were processed using the method of sol-gel, and their physical properties were evaluated using FTIR spectroscopy, XRD, SEM, VSM, and photocatalytic properties.

2. Method

2.1 Materials

The main chemicals used in the experiment are ferric nitrate nonahydrate (Merck) and citric acid monohydrate (Merck). Methylene blue (Merck) is used for photocatalytic performance under irradiation of the ultra violet light.

2.2 Synthesis of hematite (α-Fe_2O_3)

Ferric nitrate nonahydrate (0.6 M) and citric acid monohydrate (0.6 M) were used to synthesize hematite (α-Fe_2O_3). For 25 mL citric acid dissolved in distilled water, while 150 mL of iron nitrate is soluble in distilled water. The citric acid solution was added to the ferrite nitrate solution by stirring for 10 minutes at 300 rpm to ensure homogeneity. The solution is heated to a synthesis temperature of 90°C. On a hotplate, constant stirring up to a gel was performed. Then in the oven the sample was dried at 150°C for 24 hours. For 1 hour, the dry gel is ground with porcelain mortar and pestle and for 4 hours the annealing was carried out at 400°C. The others were separately annealed at 500, 600, and 700°C for 4 hours. The annealed samples were ground for 2 hours, analyzed by FTIR, XRD, SEM, and VSM, and used to determine the photocatalytic activity.

2.3 Characterization of hematite (α-Fe_2O_3)

FTIR spectroscopy (Shimadzu Prestige 21) was used to analyze chemical bonds with an analytical range of 4000–350 cm^{-1}. Transmission mode FTIR spectroscopy provides information on the molecules adsorbed on the surface. PANalytical X'Pert Pro XRD was used to evaluate the crystal structure and size of samples at 2θ in the range of 15°–80°. XRD measurements were performed and compared with the International Center for Diffraction Data (ICDD), and the size of the crystal was measured by applying an equation Debye–Scherrer based on the Miller index with the highest peak. The magnetic properties were assessed at ambient temperature using a VSM with a range of -10 kOe to 10 kOe external magnetic field. The photocatalytic properties of the hematite (α-Fe_2O_3) samples (5 mg, 10 mg, 20 mg, 30 mg, 40 mg, 50 mg and 60 mg) were observed under visible-light irradiation using 10 ppm blue methylene dye pollutants and the degradation ratio evaluate by using equation $\%D=(A_0-A_t)/A_0\mathrm{x}100\%$ where A_0 and A_t are initial absorption and after UV-Vis irradiation. Changes in the sample powder mass and irradiation time were observed at room temperature. The sample and the blue methylene dye were balanced in darkness to establish an adsorption-desorption balance for 1 hour, and the irradiation lamp was switched on. The Hitachi UH-5300 UV Spectrophotometer (with a range of wavelengths 400-800 nm) was used to monitor the degradation and absorbance of the measured sample.

3. Result and Discussion

3.1 Fourier transform infrared (FTIR) spectroscopic

FTIR spectroscopic analysis is a tool for identifying the functional groups involved in the metal oxides formation. Figure 1 shown the FTIR spectra of the synthesized hematite (α-Fe_2O_3) nanocrystals with variations in annealing temperature were recorded from 4000 cm^{-1} to 350 cm^{-1}, recognizing the bonds of the chemical and functional groups of the sample compounds28). Table 1 summarizes the absorption band (cm^{-1}) of the FTIR spectrum of hematite (α-Fe_2O_3), as illustrated in the preparation and annealed nanocrystals. Figure 1a and 1b (zoom out the metal oxide formed) show Fourier transforms infrared (FTIR) spectroscopy of the synthesized hematite (α-Fe_2O_3) powder from the sol-gel process showed non-annealing and annealing temperatures of 400°C-700°C for 4 h, respectively, and identified chemical bonds and working groups of compounds with wave numbers ranging from 350 to 4000 cm^{-1}. The wave numbers around 3455.62 cm^{-1} and 683.79 cm^{-1} is due to the elongation of a hydroxyl group (O-H) on the superficies of the nanocrystal, and the intrusion of water molecules into the environment29). The absorption bands of wavenumber k = 542.02 cm^{-1} and 450.65 cm^{-1} show modes of stretching and bending of Fe-O hematite (α-Fe2O3)30,31). The depth of the absorption peak indicates the strength of the resonance with the natural frequency of the oxide group formed.

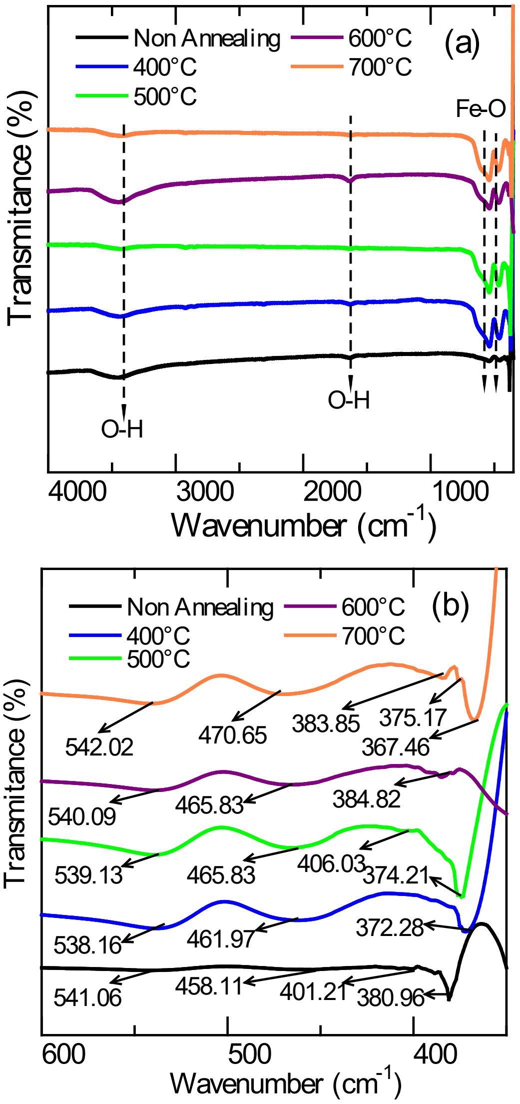

Fig. 1. The FTIR curve for sol-gel (a) hematite (α-Fe_2O_3) is for non-annealing and annealing for 4 hours at 400°C-700°C, (b) The zoomed-out figure is established on the main absorption.

Table 1. The absorption band (cm^{-1}) of the FTIR spectrum of hematite (α-Fe_2O_3) is non-annealed and annealed, and the nanocrystals show stretching, bending, asymmetrical, and symmetrical.

Hematite (α-Fe_2O_3)	(O-H) stretching	(O-H) bending	(Fe-O) asymmetric	(Fe-O) symmetric
Non-annealing	3455.62	1683.79	541.06	458.11
400°C	3437.30	1630.88	538.16	461.97
500°C	3421.87	1522.87	539.13	465.83
600°C	3448.87	1634.74	540.09	465.83
700°C	3417.04	1631.85	542.02	470.65

3.2 X-ray diffraction (XRD)

Figure 2 presents the XRD pattern of hematite (α-Fe_2O_3) nanocrystals processed by the method of sol-gel. XRD peaks in the wide-angle range of 20° to 80° with Cu Kα radiation. XRD was utilized to determine and study the structure crystalline of hematite (α-Fe_2O_3) nanocrystals produced by the sol-gel procedure. Figure 2 presents the pattern XRD of the hematite (α-Fe_2O_3) nanocrystal sample which identifies the peaks of the hematite (α-Fe_2O_3) phase and from the image, it can be seen that the resulting sample is a single-phase hematite (α-Fe_2O_3). All synthesized samples had characteristic X-ray diffraction patterns which usually correspond to the ICDD 89-0598 reference data. No other observed phase in the synthesis process was completed. ICDD reference data 89-0598 confirm that hematite (α-Fe_2O_3) crystallizes in a rhombohedral structure with space group R3c. The reflection peaks (012), (104), (110), (113), (024), (116), (112), (214), (300), (119), and (220) are hematite (α-Fe_2O_3), and the diffraction peaks are comparable with those described in ICDD 89-0598 for hematite (α-Fe_2O_3). The heat energy supplied to the atoms has the potential to reduce defects in hematite (α-Fe_2O_3) nanocrystals and improve quality. It can be found from Fig. 2 (b) as the annealing temperature rises, the material becomes crystalline. The shift in the highest peak of the XRD pattern indicates changes in the microstructure, one of which is lattice strain. As we know, the higher the annealing temperature, the better the crystal structure is obtained so that the lattice strain decreases[29].

The full width at half maximum (FWHM) of the peak reflected decreases as temperature rises. The peak width narrowed as the crystal size increased, followed by an increment in the annealing temperature. The Debye-Scherrer equation was utilized to estimate the size of the crystal of hematite (α-Fe2O3) based on the highest hkl peak (104). Table 2 presents the crystal sizes of the non-annealed hematite (α-Fe_2O_3) materials at various annealing temperatures. The size of the crystal can be seen to increase when the annealing temperature is increased. There was a change in the crystal size value from 25.9 nm to non-annealed temperatures to 34.58 nm, 39.52 nm, 39.52 nm, 41 nm, and 46.11 nm for annealing temperatures of 400°C-700°C, respectively at 4 hours. An increase in the crystal size occurs when the annealing temperature increases, which can reduce the potential crystal defects.

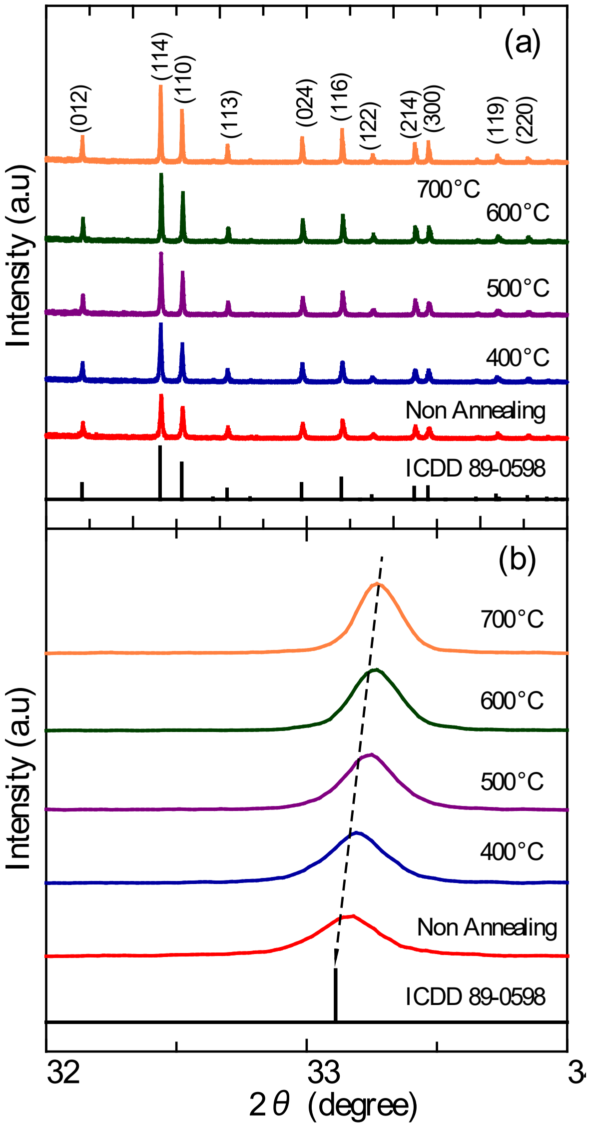

Fig. 2. Results of (a) hematite (α-Fe_2O_3) XRD patterns without and with annealing 4-hour variation at 400°C-700°C, (b) The zoomed-out number is based along the strongest peak.

Table 2. Crystallite size of hematite (α-Fe_2O_3) materials non-annealing and various annealing temperatures.

Annealing Temperature (°C)	2θ	FWHM	D (nm)
Non-annealing	33.14	0.32	25.93
400	33.21	0.24	34.58
500	33.23	0.21	39.53
600	33.25	0.20	41.51
700	33.19	0.18	46.11

3.3 Scanning electron microscopy (SEM)

The morphology and surface texture of hematite (α-Fe_2O_3) particles prepared using the sol-gel procedure were investigated using SEM analysis. The image from the SEM analyses of the synthesized hematite sample using the sol-gel procedure with a magnification of 150,000 × is presented in Fig. 3 (a) for different temperature annealing. It is clear that the synthesized sample has an irregular shape with some visible particles forming a long-length morphological pattern (like a nanopillar). Using ImageJ and Origin applications, it was determined that the average particle size distribution value was 35.95 nm, 43.63 nm, 46.97 nm, 54.42 nm and 57.89 nm for non-annealing, and annealing temperature of 400°C, 500°C, 600°C and 700°C respectively, as depicted at Fig. 3b.

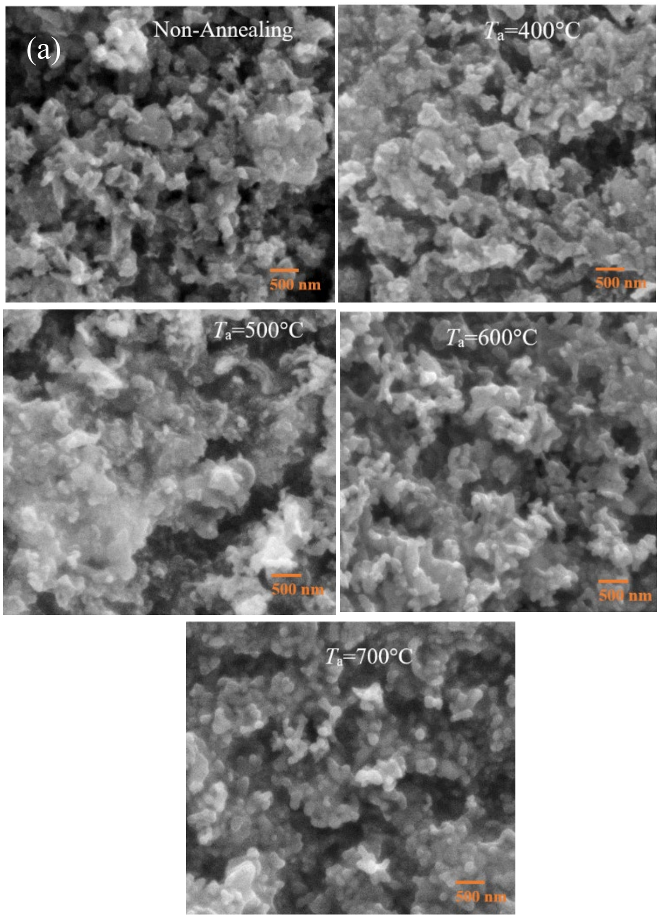

(b)

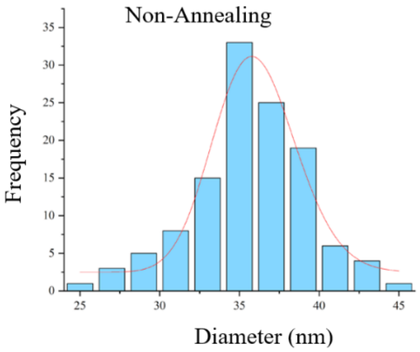

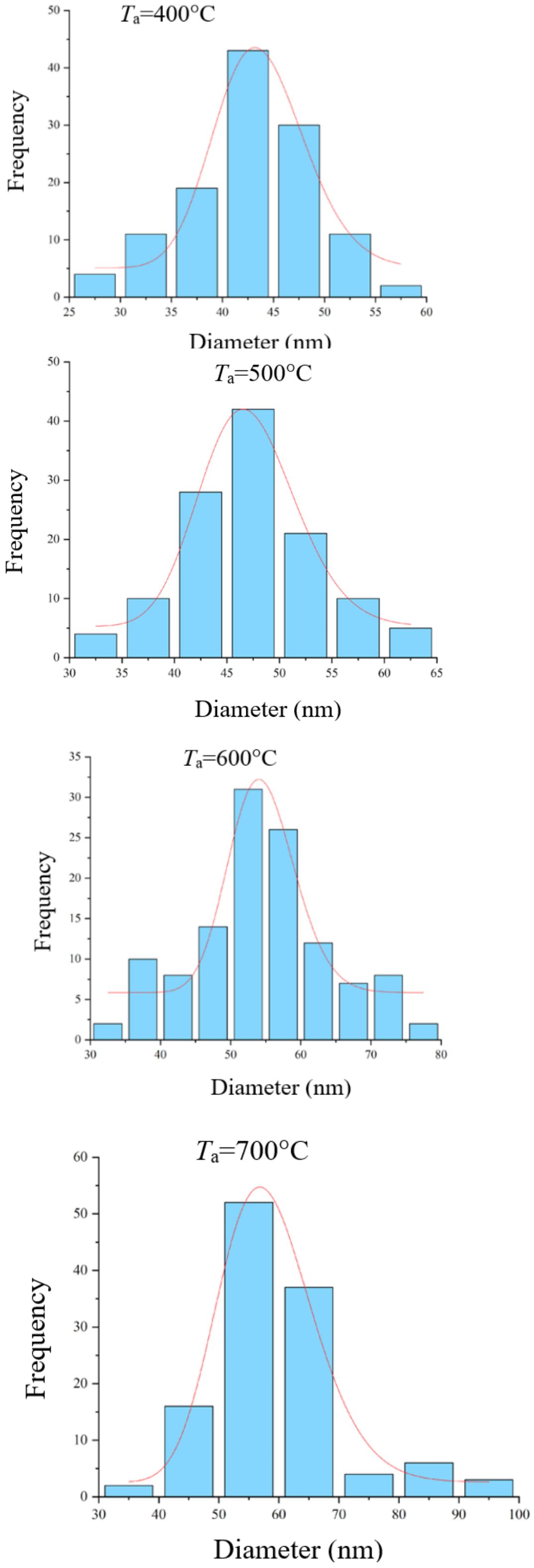

Fig. 3. (a) SEM micrographs of hematite (α-Fe_2O_3) nanocrystals and (b) particle size distribution hematite (α-Fe_2O_3) samples for non-annealed and annealed of 400°C, 500°C, 600°C, 700°C.

3.4 Vibrating sample magnetometer (VSM)

Using a vibrating sample magnetometer, the magnetic characteristics of hematite (α-Fe_2O_3) samples were investigated. Figure 4 shows the loop hysteresis in the form of the M-H curve of the hematite (α-Fe_2O_3) nanocrystals in the observed magnetic field at room temperature. Table 3 shows the magnetics parameters obtained by the VSM analysis, data for saturation magnetization (*Ms*), persistence magnetization (*Mr*), and coercive force (*Hc*). The *Ms* value for the non-annealed hematite (α-Fe_2O_3) samples was 2.093 emu/g, and when treated with annealing temperatures of 400–700 °C for 4 h, the *Ms* value decreased by 0.590 emu/g, 0.306 emu/g, 0.272 emu/g, and 0.414 emu/g, respectively.

Increasing the annealing temperature seems to change the cation distribution with no trend. Meanwhile, increasing the annealing temperature increases the crystallite size. If the crystallite size is directly correlated with the particle size, then the change in the *Hc* value increases to a maximum of 1.96 kOe, indicating that the single domain state is obtained. And thereafter *Hc* decreases with the increase in crystallite size due to multi domain formation. Here, the single or multidomain formation is difficult to explained due to impact many aspects such kind surface defects, crystal structure, crystal size, shape, domain wall pinning, and surface charge[32-34)].

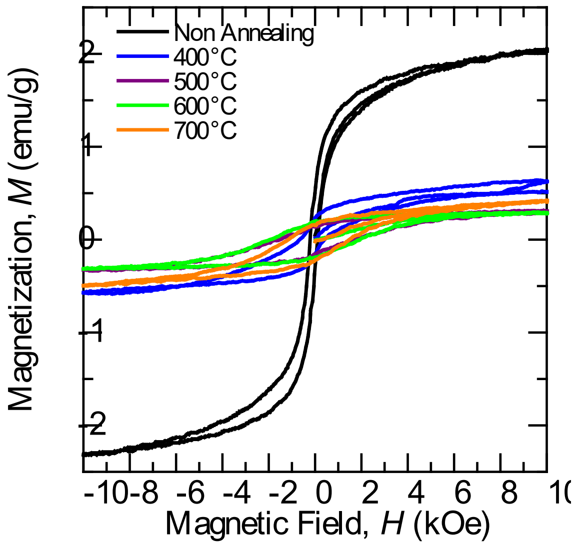

Fig. 4. hematite (α-Fe_2O_3) hysteresis curves without annealed and annealed for the 4 hours various of 400°C-700°C using the sol-gel procedure.

Table 3. Magnetic parameters of hematite (α-Fe_2O_3) at non-annealing and various annealing temperatures.

Annealing (°C)	H_c (Oe)	M_s (emu/g)	M_r (emu/g)	K (erg/cm^3)
Non-Ann	170.01	2.09	0.59	370.63
400	547.93	0.59	0.20	336.54
500	1662.62	0.31	0.15	530.64
600	1965.72	0.27	0.19	557.23
700	1323.61	0.41	0.19	570.80

3.5 Ultraviolet-visible spectroscopy (UV-Vis) studies

Hematite (α-Fe_2O_3) samples were prepared for ultraviolet-visible (UV-Vis) spectroscopy of hematite (α-Fe_2O_3) nanocrystals using the sol-gel method at annealing temperatures of 400°C-700°C for 4 h. The absorption spectrum was captured using the Hitachi UH-5300 UV-Vis spectrophotometer at ambient temperature. The photocatalytic performance of hematite (α-Fe_2O_3) was assessed by the photocatalytic reduction of the blue methylene pollutant[35-39)] at 10 ppm under visible-light irradiation.

The catalyst sample was dispersed in 10 mL of blue methylene, and the effect of changes in the mass of the sample powder and the time of visible light irradiation at room temperature was investigated. Figure 5 presents several factors that affect the value of the degradation of blue methylene. Figure 5 (a) shows that the annealing temperature affects the magnitude of the degradation of blue methylene in hematite (α-Fe_2O_3) material, as present in Table 4. In this case, the addition of annealing temperature caused the degradation value of blue methylene to be smaller. This could be attributed to the larger hematite (α-Fe2O3) crystal size when the temperature was increased, which was confirmed by the XRD data. The small and large sizes of the crystals affect the size of the particle pores. The pore size distribution affects the size distribution of the adsorbate molecules entering the adsorbent particles. Regarding the effect of pore size, a smaller pore size indicates higher photocatalytic activity[40)].

Table 4. The calculated degradation of hematite (α-Fe_2O_3) non-annealing and with annealing variation.

No.	Hematite (α-Fe_2O_3) with mass 10 mg	
	Annealing Temperature (°C)	Irradiation 10 Minutes (%D)
1	Non-annealing	36.43
2	400	28.62
3	500	27.63
4	600	23.17
5	700	22.31

Table 5. The calculated degradation of hematite (α-Fe_2O_3) non-annealing affected mass variation.

No.	Hematite (α-Fe_2O_3) Non-annealing	
	Massa (mg)	Irradiation 10 Minutes %D
1	5	31.47
2	10	36.43
3	20	47.83
4	40	80.67
5	60	90.05

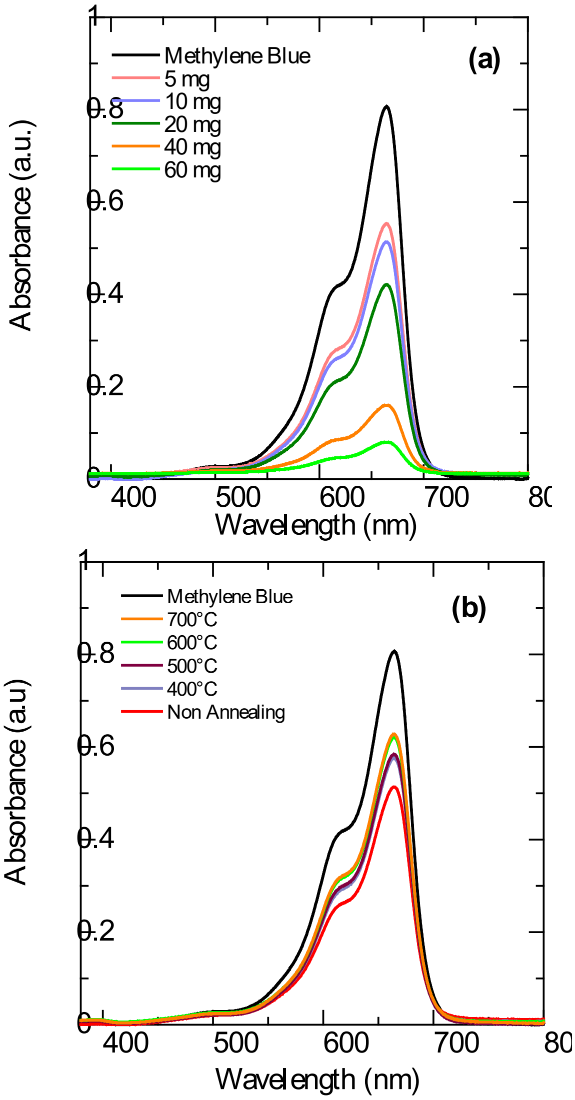

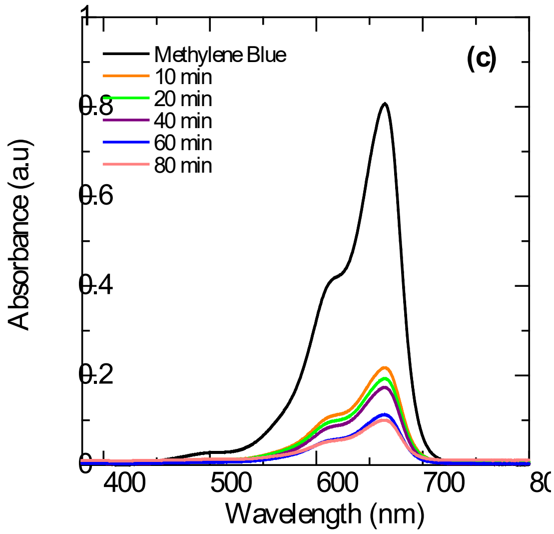

Fig. 5. UV-Vis curve of blue methylene photodegradation using hematite (α-Fe2O3) nanocrystal for (a) change in annealing temperature, (b) variation of mass for sample without annealing, and (c) modification of time UV irradiated for sample without annealing.

Figure 5 (b) and Table 5 show that the addition of hematite (α-Fe_2O_3) also affects the degradation of blue methylene. It can be found out that addition of samples of 40 mg and 60 mg had a significant effect on the degradation of blue methylene (80.67% and 90.04%) compared to other doses. Increasing the catalyst dosage increased the response rate as the available active area increased. The irradiation duration can also affect the degradation of MB, as shown in Fig. 5 (c). As the irradiation time increased, radical formation increased at a higher rate. The irradiation time is the length of the interaction between the UV light and the photocatalyst in producing •OH radicals. Furthermore, it influences the duration of contact between •OH and the degraded dye. The longer the irradiation time, the higher is the photon energy produced. The resulting increase in photon energy produces an increasing amount of radical •OH. •OH radicals are strong oxidizing agents that can be used to degrade dyestuffs. The greater the amount of •OH produced, the greater the degradation of the dye will be degraded. Electrons move from the valence band to the conduction band, leaving holes in the valence band behind, when photons with energy above the catalyst's band gap are absorbed by the catalyst. This is the beginning of the mechanism of photocatalytic dye degradation. The catalytic surface in the conductive band has access to excited electrons. In the initial stage of dye degradation, dye molecules are taken up by the catalyst's surface. The available O_2 then reacts with the surface's electrons and holes (either from the air or pure oxygen added) and H_2O to obtain superoxide radicals ($•O_2^-$) and hydroxyl radicals (•OH), respectively. Then, these two radicals target the dye's structure and chromosphere to create excited intermediates that eventually degrade more straightforward coloured molecules such as H_2O, CO_2, and other fragments[41,43].

In addition, the photocatalytic mechanism of MB degradation using hematite nanoparticles was proposed following the mechanism[43]. When UV light hits a hematite sample, the excited electrons jump from the valence band (VB) to the conduction band (CB) leaving holes. Photogenerated holes can recombine with water on the surface of the photocatalyst to produce reactive hydroxyl radicals (•OH) and H+ ions which are seen as the main photocatalytic mechanism. Moreover, the hole in VB can recombine with OH-, to realize a radical (•OH). Photogenerated e- from the conduction band (CB) reacts with oxygen to produce the super radical (•O2−). Hydroxyl radical (•OH) and superoxide (•O2−) will react with the dye pollutants to degrade dye pollutants. Overall, it is illustrated with a typical photocatalyst reaction equation below.

$$Fe_2O_3 + h\nu \rightarrow Fe_2O_3 + \mathrm{h}^+_{\mathrm{VB}} + \mathrm{e}^-_{\mathrm{CB}}$$

$$Fe_2O_3(h^+_{\mathrm{VB}}) + \mathrm{H}_2O \rightarrow \mathrm{OH}^\bullet + \mathrm{H}^+ + Fe_2O_3$$

$$Fe_2O_3\ (h^+_{\mathrm{VB}}) + \mathrm{OH}^- \rightarrow \mathrm{OH}^\bullet + \alpha - Fe_2O_3$$

$$\alpha - Fe_2O_3\ (e^-_{\mathrm{CB}}) + \mathrm{O}_2 \rightarrow {}^\bullet O_2^-$$

$$\mathrm{OH}^\bullet + \mathrm{MB} \rightarrow \mathrm{CO}_2 + \mathrm{H}_2O$$

$${}^\bullet O_2^- + \mathrm{MB} \rightarrow \mathrm{CO}_2 + \mathrm{H}_2O \qquad \text{(degradation process)}$$

4. Conclusion

Hematite (α-Fe2O3) nanocrystals were successfully processed using the sol-gel method. The XRD result confirmed that the crystalline structure of hematite is a rhombohedral structure. The crystallite size increase with the increase of temperature annealing. The methylene blue photodegradation sensitive with the increase of the hematite nanocrystal and the highest degradation efficiency of blue methylene 90.04% is obtained for using without annealing sample of 60 mg under 10 minutes irradiation. Here the reduction of the dye support by surface adsorption following the photocatalysis mechanism should be addressed for the dye removal mechanism.

Acknowledgments

This study received funding from Penelitian Unggulan Terapan Universitas Sebelas Maret Surakarta with contract number: 254/UN27.22/PT.01.03/2022.

References

1) Walter, D. (2006). Characterization of synthetic hydrous hematite pigments. *Thermochimica acta*, *445*(2), 195-199. https://doi.org/10.1016/j.tca.2005.08.011
2) Prim, S. R., Folgueras, M. V., De Lima, M. A., & Hotza, D. (2011). Synthesis and characterization of hematite pigment obtained from a steel waste industry. *Journal of hazardous materials*, *192*(3), 1307-1313. https://doi.org/10.1016/j.jhazmat.2011.06.034
3) Wu, C., Yin, P., Zhu, X., OuYang, C., & Xie, Y. (2006). Synthesis of hematite (α-Fe_2O_3) nanorods: diameter-size and shape effects on their applications in magnetism, lithium ion battery, and gas sensors. *The Journal of Physical Chemistry B*, *110*(36), 17806-17812. https://doi.org/10.1016/j.jhazmat.2011.06.034
4) X. Gou, G.Wang, J. Park, H. Liu and J. Yang, Monodisperse hematite porous nanospheres: synthesis, characterization, and applications for gas sensors, Nanotechnology, 2008, 19, 125606–125612. https://doi.org/10.1088/0957-4484/19/12/125606
5) Tilley, S. D., Cornuz, M., Sivula, K., & Grätzel, M. (2010). Light‐induced water splitting with hematite: improved nanostructure and iridium oxide catalysis. *Angewandte Chemie International Edition*, *49*(36), 6405-6408. https://doi.org/10.1002/ange.201003110
6) Zhang, H. J., Meng, F. N., Liu, L. Z., & Chen, Y. J. (2019). Convenient route for synthesis of alpha-Fe_2O_3 and sensors for H2S gas. *Journal of Alloys and Compounds*, *774*, 1181-1188. https://doi.org/10.1016/j.jallcom.2018.09.384
7) Xu, Y., Zhang, G., Du, G., Sun, Y., & Gao, D. (2013). α-Fe_2O_3 nanostructures with different morphologies: additive-free synthesis, magnetic properties, and visible light photocatalytic properties. *Materials Letters*, *92*, 321-324.
8) Tartaj, P., Morales, M. P., Gonzalez-Carreño, T., Veintemillas-Verdaguer, S., & Serna, C. J. (2011). The iron oxides strike back: from biomedical applications to energy storage devices and photoelectrochemical water splitting.
9) Zeng, S., Tang, K., Li, T., Liang, Z., Wang, D., Wang, Y., & Zhou, W. (2007). Hematite hollow spindles and microspheres: selective synthesis, growth mechanisms, and application in lithium ion battery and water treatment. *The Journal of Physical Chemistry C*, *111*(28), 10217-10225.
10) Thomann, I., Pinaud, B. A., Chen, Z., Clemens, B. M., Jaramillo, T. F., & Brongersma, M. L. (2011). Plasmon enhanced solar-to-fuel energy conversion. *Nano letters*, *11*(8), 3440-3446.
11) Chen, J., Xu, L., Li, W., & Gou, X. (2005). α‐Fe_2O_3 nanotubes in gas sensor and lithium‐ion battery applications. *Advanced Materials*, *17*(5), 582-586.
12) Wen, X., Wang, S., Ding, Y., Wang, Z. L., & Yang, S. (2005). Controlled growth of large-area, uniform, vertically aligned arrays of α-Fe_2O_3 nanobelts and nanowires. *The Journal of Physical Chemistry B*, *109*(1), 215-220.
13) Woo, K., Lee, H. J., Ahn, J. P., & Park, Y. S. (2003). Sol–gel mediated synthesis of Fe_2O_3 nanorods. *Advanced Materials*, *15*(20), 1761-1764.

14) Wu, Y., & Wang, X. (2011). Preparation and characterization of single-phase α-Fe_2O_3 nano-powders by Pechini sol–gel method. *Materials Letters*, *65*(13), 2062-2065.

15) Fernandes, D. M., Hechenleitner, A. W., Silva, M. F., Lima, M. K., Bittencourt, P. S., Silva, R., & Pineda, E. G. (2009). Preparation and characterization of NiO, Fe_2O_3, NiO. and FeO. O_3ZnO. 97O nanoparticles. *Materials Chemistry and Physics*, *118*(2-3), 447-452.

16) Yang, P., Wang, D., Zhao, J., & Shi, R. (2015). Facile synthesis of hematite nanoplates and their self-assembly generated by domain growth of NaCl. *Materials Research Bulletin*, *65*, 36-41.

17) Radu, T., Iacovita, C., Benea, D., & Turcu, R. (2017). X-ray photoelectron spectroscopic characterization of iron oxide nanoparticles. *Applied Surface Science*,*405*, 337-343.

18) Chen, L., Lin, Z., Zhao, C., Zheng, Y., Zhou, Y., & Peng, H. (2011). Direct synthesis and characterization of mesoporous Fe_3O_4 through pyrolysis of ferric nitrate-ethylene glycol gel. *Journal of Alloys and Compounds*, *509*(1), L1-L5.

19) S. Yang, Y.-H. Jang, C. H. Kim et al., "A flame metal combustion method for production of nanoparticles," Powder Technology, vol. 197, no. 3, pp. 170–176, 2010.

20) Jesus, J. R., Lima, R. J. S., Moura, K. O., Duque, J. G. S., & Meneses, C. T. (2018). Anisotropic growth of α-Fe_2O_3 nanostructures. *Ceramics International*, *44*(4), 3585-3589.

21) Muhammad, M., Fatmaliana, A., & Jalil, Z. (2019). Study of hematite mineral (Fe2O3) extracted from natural iron ore prepared by co-precipitation method. IOP Conference Series: Earth and Environmental Science, 348(1), 012135. https://doi.org/10.1088/1755-1315/348/1/012135

22) Jalil, Z., Rahwanto, A., Mulana, F., & Handoko, E. (2019). Synthesis of nano-hematite (Fe2O3) extracted from natural iron ore prepared by mechanical alloying method. AIP Conference Proceedings. https://doi.org/10.1063/1.5124671

23) Rasheed, R. T., Al-Algawi, S. D., Kareem, H. H., & Mansoor, H. S. (2018). Preparation and characterization of hematite iron oxide (α-Fe_2O_3) by sol-gel method. *Chem Sci J*, *9*(197), 2.

24) Kotsikau D, Ivanovskaya M (2011) Advanced metaloxide nanomaterials for gas sensors with controlled properties. Sci Technol Sci 1: 1-6.

25) Mallick, P., & Dash, B. N. (2013). X-ray diffraction and UV-visible characterizations of α-Fe_2O_3 nanoparticles annealed at different temperature. *Nanosci. Nanotechnol*, *3*(5), 130-134.

26) Mammah, S. L., Opara, F. E., Sigalo, F. B., Ezugwu, S. C., & Ezema, F. I. (2012). Effect of concentration on the optical and solid state properties of ZnO thin films deposited by Aqueous Chemical Growth (ACG) method. *Journal of Modern Physics*,*3*(10), 1516.

27) Goudjil, M. B., Dali, H., Zighmi, S., Mahcene, Z., & Bencheikh, S. E. (2024). Photocatalytic degradation of methylene blue dye with biosynthesized Hematite α-Fe2O3 nanoparticles under UV-Irradiation. Desalination and Water Treatment, 100079. https://doi.org/10.1016/j.dwt.2024.100079

28) Farahmandjou, M., & Soflaee, F. (2015). Synthesis and characterization of α-Fe_2O_3 nanoparticles by simple co-precipitation method. *Physical Chemistry Research*, *3*(3), 191-196.

29) Archana, V., Joseph Prince, J., & Kalainathan, S. (2021). Simple one-step leaf extract-assisted preparation of α-Fe_2O_3 nanoparticles, physicochemical properties, and its sunlight-driven photocatalytic activity on methylene blue dye degradation. *Journal of Nanomaterials*, *2021*.

30) Petcharoen, K., & Sirivat, A. J. M. S. (2012). Synthesis and characterization of magnetite nanoparticles via the chemical co-precipitation method. *Materials Science and Engineering: B*, *177*(5), 421-427.

31) Utari, Maulidina, H., Arilasita, R., Widiyandari, H., Suharno, & Purnama, B. (2023). Citric acid concentration tune of structural and magnetic properties in hematite (α−Fe2O3) nanoparticles synthesized by sol−gel method. Materials Research Express, 10(3), 036101. https://doi.org/10.1088/2053-1591/acbf0c

32) Zong, Y., Sun, Y., Meng, S., Wang, Y., Xing, H., Li, X., & Zheng, X. (2019). Doping effect and oxygen defects boost room temperature ferromagnetism of Co-doped ZnO nanoparticles: experimental and theoretical studies. *RSC advances*, *9*(40), 23012-23020.

33) Sayed, F. N., & Polshettiwar, V. (2015). Facile and sustainable synthesis of shaped iron oxide nanoparticles: effect of iron precursor salts on the shapes of iron oxides. *Scientific reports*, *5*(1), 1-14.

34) Wu, J., Mao, S., Ye, Z. G., Xie, Z., & Zheng, L. (2010). Room-temperature weak ferromagnetism induced by point defects in α-Fe_2O_3. *ACS Applied Materials & Interfaces*, *2*(6), 1561-1564.

35) Ezaki, M., & Kusakabe, K. (2014). Highly crystallized tungsten trioxide loaded titania composites prepared by using ionic liquids and their photocatalytic behaviors, Evergreen, 1(2), 18–24. https://doi.org/10.5109/1495159.

36) Azani, A., Halin, D. S. C., Abdullah, M. M. A. B., Razak, K. A., Razak, M. F. S. A., din Ramli, M. M., & Chobpattana, V. (2021). The Effect of GO/TiO_2 Thin Film During Photodegradation of Methylene Blue Dye, Evergreen, 8(3), 556–564. https://doi.org/10.5109/4491643.

37) Nugrahaningtyas, K. D., Suharbiansah, R. S., Lestari, W. W., & Rahmawati, F. (2022). Metal Phase, Electron Density, Textural Properties, and Catalytic Activity of CoMo Based Catalyst Applied in

Hydrodeoxygenation of Oleic Acid, Evergreen, 9(2), 283–291. https://doi.org/10.5109/4793665.

38) Zamri, N. I. I., Zulmajdi, S. L. N., Kusrini, E., Ayuningtyas, K., Yasin, H. M., & Usman, A. (2020). *Rhodamine b photocatalytic degradation using cuo particles under uv light irradiation for applications in industrial and medical fields* (Doctoral dissertation, Kyushu University), Evergreen, 7(2), 280–284. https://doi.org/10.5109/4055233
39) Al Hijri, H., Fatriansyah, J. F., Sofyan, N., & Dhaneswara, D. (2022). Potential Use of Corn Cob Waste as the Base Material of Silica Thin Films for Anti-Reflective Coatings, Evergreen, 9(1), 102–108. https://doi.org/10.5109/4774221
40) He, K., Zhao, C., Zhao, G., & Han, G. (2015). Effects of pore size on the photocatalytic activity of mesoporous TiO_2 prepared by a sol–gel process. *Journal of Sol-Gel Science and Technology*, *75*(3), 557-563.
41) Shah, P., Unnarkat, A., Patel, F., Shah, M., & Shah, P. (2022). A comprehensive review on spinel based novel catalysts for visible light assisted dye degradation. *Process Safety and Environmental Protection*, *161*, 703-722.
42) Naimah, M. T., Pratama, F. D. N., & Ibadurrohman, M. (2022). Photocatalytic Hydrogen Production Using Fe-Graphene/TiO_2 Photocatalysts in the Presence of Polyalcohols as Sacrificial Agents, Evergreen, 9(4), 1244–1251. https://doi.org/10.5109/6625736
43) Hmamouchi, S., El Yacoubi, A., & El Idrissi, B. C. (2022). Using egg ovalbumin to synthesize pure α-Fe2O3 and cobalt doped α-Fe2O3: structural, morphological, optical and photocatalytic properties. Heliyon, 8(2).